CHEMISTRY
A EUROPEAN JOURNAL

DOI: 10.1002/chem.200600303

A New Basic Motif in Cyanometallate Coordination Polymers: Structure and Magnetic Behavior of $M(\mu\text{-}OH_2)_2[Au(CN)_2]_2$ (M = Cu, Ni)

Julie Lefebvre,[a] Fergal Callaghan,[b] Michael J. Katz,[a] Jeff E. Sonier,*[b, c] and Daniel B. Leznoff*[a]

Abstract: The structures of two cyanoaurate-based coordination polymers, $M(\mu\text{-}OH_2)_2[Au(CN)_2]_2$ (M = Cu, Ni), were determined by using a combination of powder and single-crystal X-ray diffraction techniques. The basic structural motif for both polymers contains rarely observed $M(\mu\text{-}OH_2)_2M$ double aqua-bridges, which generate an infinite chain; two *trans* $[Au(CN)_2]^-$ units also dangle from each metal center. The chains form ribbons that interact three dimensionally through CN···H hydrogen bonding. The magnetic properties of both compounds and of the dehydrated analogue $Cu[Au(CN)_2]_2$ were investigated by direct current (dc) and alternating current (ac) magnetometry; muon spin-relaxation data was also obtained to probe their magnetic properties in zero-field. In $M(\mu\text{-}OH_2)_2[Au(CN)_2]_2$, ferromagnetic chains of $M(\mu\text{-}OH_2)_2M$ are present below 20 K. Interchain magnetic interactions mediated through hydrogen bonding, involving water and cyanoaurate units, yield a long-range magnetically ordered system in $Cu(\mu\text{-}OH_2)_2[Au(CN)_2]_2$ below 0.20 K, as indicated by precession in the muon spin polarization decay. $Ni(\mu\text{-}OH_2)_2[Au(CN)_2]_2$ undergoes a transition to a spin-glass state in zero-field at 3.6 K, as indicated by a combination of muon spin-relaxation and ac-susceptibility data. This transition is probably due to competing interactions that lead to spin frustration. A phase transition to a paramagnetic state is possible for $Ni(\mu\text{-}OH_2)_2[Au(CN)_2]_2$ upon application of an external field; the critical field was determined to be 700 Oe at 1.8 K. The dehydrated compound $Cu[Au(CN)_2]_2$ shows weak antiferromagnetic interactions at low temperatures.

Keywords: aqua-bridged chains · aurophilicity · coordination polymers · magnetic properties · muon spin relaxation

Introduction

The intense interest in coordination polymer research can be attributed to the potential to design functional materials[1] by utilizing judiciously chosen building blocks to generate specific structural motifs with targeted physical properties.[2,3] The cyanometallate-based $Fe_4[Fe(CN)_6]_3{\cdot}14H_2O$ material, better known as Prussian Blue, is perhaps the oldest known coordination polymer and occupies a special place in this field. Although prepared initially by Diesbach in 1704,[4] its structure remained a mystery for several centuries, partly due to the extreme difficulty in preparing single crystals, until powder[5] and eventually single-crystal X-ray diffraction data reported in 1972 revealed the basic structural motif (Figure 1a): a three-dimensional cubic array of Fe^{II}-CN-Fe^{III} bridges with random vacant lattice sites containing $Fe{-}OH_2$ units, and the remaining H_2O molecules occupying the channel-pore space.[6]

This structure has been a source of great inspiration in the field of coordination polymers. By exploiting the modu-

[a] J. Lefebvre, M. J. Katz, Prof. D. B. Leznoff
Department of Chemistry, Simon Fraser University
8888 University Drive, Burnaby, BC, V5A 1S6 (Canada)
Fax: (+1) 604-291-3765
E-mail: dleznoff@sfu.ca

[b] Dr. F. Callaghan, Prof. J. E. Sonier
Department of Physics, Simon Fraser University
8888 University Drive, Burnaby, BC, V5A 1S6 (Canada)
Fax: (+1) 604-291-3592
E-mail: jsonier@sfu.ca

[c] Prof. J. E. Sonier
Canadian Institute for Advanced Research
Toronto, Ontario, M5G 1Z8 (Canada)

Supporting information for this article is available on the WWW under http://www.chemeurj.org/ or from the author: Tables contain TGA data and reflection positions and intensities from the powder diffractograms of **1** and **2**, and fractional coordinates for the atoms in the proposed ribbon model. Figures show the extended structure in the sheet and ribbon models, their predicted powder diffractograms, and powder diffractograms of **1** and **1a**.

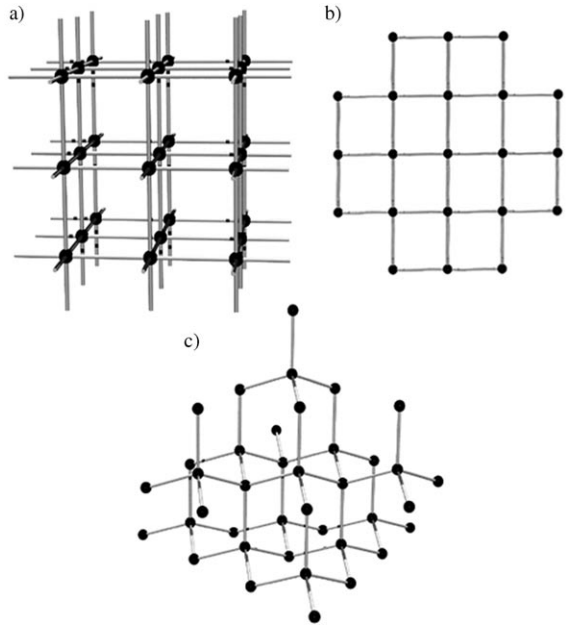

Figure 1. Basic structural motifs: a) cubic, b) square-grid, c) diamond-like arrays.

lar nature of coordination polymer synthesis, whereby each building block can be independently modified and chosen to express a particular physical property, the two iron-metal sites of Prussian Blue have been systematically substituted for other metals, with the basic three-dimensional structural motif remaining essentially unchanged. Prussian Blue ferromagnetically orders at 5.6 K,[7] and extensive studies on these metal-substituted analogues were conducted in a drive to generate materials that magnetically order at higher temperatures.[2,8] Other modifications of the Prussian Blue system have yielded porous materials that show significant H_2-uptake[9] or vapochromic behavior.[10]

A more-substantial modular substitution is the alteration of the key Prussian Blue building block, namely the octahedral cyanometallate $[M(CN)_6]^{n-}$, for nonoctahedral cyanometallates $[M(CN)_x]^{y-}$; this has generated a series of other "basic structural motifs" that have served as points of reference for further modification and research.[11–13] For example, four-coordinate square-planar $[M(CN)_4]^{2-}$ (M = Ni, Pd, Pt) building blocks were found to generate square-grid arrays (Hoffmann-clathrate type, Figure 1b) with transition-metal cations,[13,14] whereas their reaction with tetrahedral cyanometallate units (M = Zn, Cd) favour the formation of three-dimensional diamond-like networks (Figure 1c).[15] With seven- or eight-coordinate cyanometallates, such as $[Mo(CN)_7]^{4-}$ and $[Mo/W(CN)_8]^{4-}$, and transition-metal cations, three-dimensional networks can also be obtained.[16]

The use of *linear* cyanometallates, such as $[Au(CN)_2]^-$, in coordination polymers has been particularly sparse,[17] despite the greater range of possible structural motifs inherent with a linear building block. In addition, $[Au(CN)_2]^-$ has the ability to increase structural dimensionality, stability, and complexity through the formation of gold–gold (aurophilic) interactions.[18–21] Several familiar structural motifs have been identified amongst simple (i.e., ancillary ligand-free) $[Au(CN)_2]$-containing coordination polymers. Pseudocubic Prussian Blue type structures of the form $KM[Au(CN)_2]_3$ (M = Fe,[22] Co[23]), interpenetrated three-dimensional quartz-like arrays, as in $Co[Au(CN)_2]_2$[24] and $Zn[Au(CN)_2]_2$,[25] or square-planar sheets, as in $Mn[Au(CN)_2]_2{\cdot}2H_2O$,[22] have all been reported. A series of complex three-dimensional arrays of $Ln[Au(CN)_2]_3{\cdot}2{,}3H_2O$ (Ln = La, Gd, Sm, Eu, Tb, Dy) have also been prepared.[26] Similar to the situation for Prussian Blue and its many analogues, despite an aqueous synthesis, these $[Au(CN)_2]$-based products either do not retain water at all, or the water molecules bind to the metal cation without significantly impacting the basic structural motif.

As part of our ongoing investigations into d^{10}-cyanometallate-based coordination polymers and their materials properties,[19,27,28] we recently described the synthesis and vapochromic properties of $Cu[Au(CN)_2]_2(DMSO)_2$ and its H_2O analogue, $Cu(H_2O)_2[Au(CN)_2]_2$ (**1**).[29] Although a series of structures of solvent adducts were described, no structural details were reported for **1**, due to the inherent difficulties in obtaining crystals of X-ray diffraction quality for such ligand-free systems. However, by using a combination of powder and single-crystal X-ray diffraction techniques, we have now determined and hereby report the structure of this "simple" ligand-free cyanoaurate-based coordination polymer (**1**) and its nearly isostructural nickel(II) analogue, $Ni(H_2O)_2[Au(CN)_2]_2$ (**2**). Both compounds have a very unusual basic structural motif in which the water molecules play the key structural role; the structure type is unique with respect to cyanometallate-based polymers and, more broadly, is rare in aqueous coordination chemistry.

Because the structural motif often defines the physical properties (e.g., magnetism) of a particular compound, the magnetic behavior of $Cu(\mu\text{-}OH_2)_2[Au(CN)_2]_2$ (**1**) and $Ni(\mu\text{-}OH_2)_2[Au(CN)_2]_2$ (**2**), and the related dehydrated $Cu[Au(CN)_2]_2$ (**1a**) polymer, were investigated by direct current (dc) and alternating current (ac) superconducting quantum interference device (SQUID) magnetometry. To obtain further information on the magnetic properties of these systems, particularly in zero-applied field, the muon spin-relaxation (μSR) technique was also applied.[30] The μSR method involves the implantation of short-lived, nearly 100% spin-polarized muons into the sample. The time evolution of the muon spin polarization reflects the local magnetic field at the muon stopping site(s). In contrast to bulk magnetic susceptibility, μSR is a local magnetic probe that is highly sensitive to weak internal magnetic fields, short-range magnetic order, and disordered magnetism. Furthermore, μSR is sensitive to spin fluctuation rates in the range 10^4–10^{12} Hz, which is beyond the range accessible with ac-susceptibility magnetometry. Recently, μSR has been applied to the study of molecule-based low-dimensional magnets,[31] including transition-metal–dicyanamide polymers[32] and layered organic and inorganic hybrid systems.[33]

Results

Synthesis and chemical characterization: The addition of an aqueous solution of $K[Au(CN)_2]$ (two equivalents) to an aqueous solution of $Cu(ClO_4)_2{\cdot}6H_2O$ (one equivalent) generates immediately a green precipitate with the empirical formula $Cu(H_2O)_2[Au(CN)_2]_2$ (**1**) in high yield.[29] The analogous reaction with $Ni(NO_3)_2{\cdot}6H_2O$ yields blue-green $Ni(H_2O)_2[Au(CN)_2]_2$ (**2**). The infrared spectra of **1** and **2** are similar. Bands for the cyanide stretching frequencies (ν_{CN}) are observed at 2217 (s), 2194 (vw), and 2171 (s) cm^{-1} for **1**, and at 2214 (s), 2204 (sh), and 2170 (s) cm^{-1} for **2**. The ν_{CN} frequencies of compounds **1** and **2** are blue-shifted relative to the 2141 cm^{-1} stretch of $K[Au(CN)_2]$, consistent with binding of *N*-cyano groups to the transition-metal centers.[11]

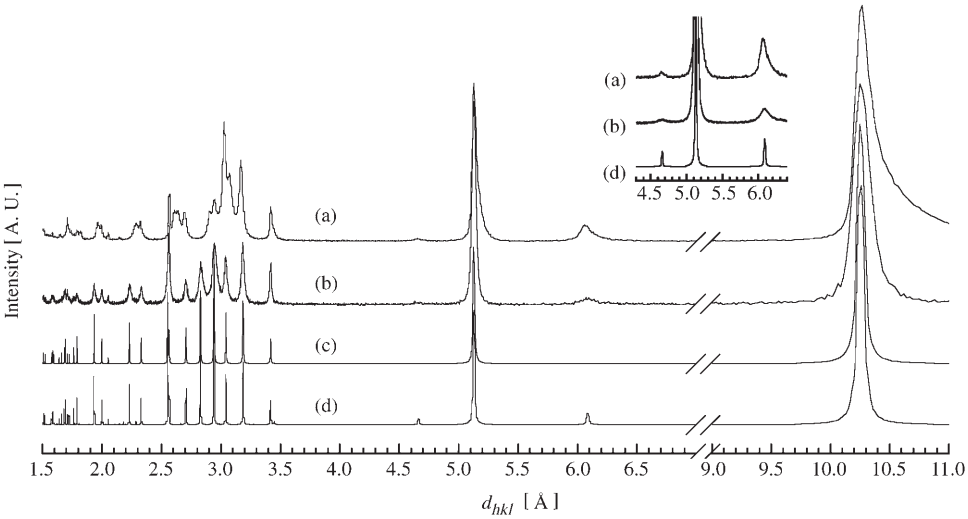

Figure 2. Powder X-ray diffractograms recorded for a) $Cu(\mu\text{-}OH_2)_2[Au(CN)_2]_2$ (**1**) and b) $Ni(\mu\text{-}OH_2)_2[Au(CN)_2]_2$ (**2**), and powder X-ray diffractograms predicted for **2** from c) initial single-crystal structure solution and d) the proposed ribbon model obtained by doubling the *c* axis.

Thermogravimetric analysis (TGA) of compounds **1** and **2** showed that the water molecules are lost within the temperature ranges of 145–180 °C and 215–260 °C, respectively (Table S1, Supporting Information). Anhydrous green-brown $Cu[Au(CN)_2]_2$ (**1a**) was prepared in bulk by thermally removing the water molecules from **1** at 180 °C for several hours. The IR spectrum of **1a** shows only one cyanide stretching frequency (2191 cm^{-1}). By monitoring the infrared spectra and color of **1a** as a function of time, it was evident that rehydration back to **1** occurred after several hours under ambient atmospheric conditions.

Structural characterization: The ν_{CN} frequencies of $[Au(CN)_2]$-based coordination polymers are extremely sensitive to small chemical and structural changes, and can be used to discriminate between different compounds.[29,34] Thus, the similar pattern and small positional differences observed between the ν_{CN} frequencies of **1** and **2** strongly suggest that the $[Au(CN)_2]^-$ units have almost identical environments in these two compounds. In addition, the powder X-ray diffractograms of **1** and **2** were collected (Figure 2) and are almost superimposable. The similarities in the stretching frequencies and the powder diffractograms suggest that these compounds are nearly isostructural.

The growth of crystals of **1** and **2** suitable for single-crystal X-ray studies was very challenging. Attempts at crystal growth by using H-shaped tubes, gel-diffusion techniques, layered solvents, and more-standard variations of concentration and temperature in water or water/solvent mixtures generated only microcrystalline powder. However, small poor-quality crystals of **2** (less than 0.05 mm per side), used to collect single-crystal X-ray data, were obtained by hydrothermal recrystallization; these crystals and the bulk powder had comparable infrared and combustion data. The cell parameters determined for **2** are presented in Table 1.

Table 1. Unit cell parameters for $Cu(\mu\text{-}OH_2)_2[Au(CN)_2]_2$ (**1**) and $Ni(\mu\text{-}OH_2)_2[Au(CN)_2]_2$ (**2**).

	1	**2**	**2**
sample	powder	initial single crystal	powder and single crystal
crystal system	monoclinic	orthorhombic	orthorhombic
space group	*P*2 or *P*2/*m*	*Cmmm*	*Immm*
a [Å]	6.335	6.375(3)	6.374(3)
b [Å]	20.509	3.3186(11)	3.3183(11)
c [Å]	3.482	10.252(2)	20.512(5)
α [°]	90	90	90
β [°]	90.93	90	90
γ [°]	90	90	90
V [$Å^3$]	452.324	216.89(13)	433.9(3)

From initial single-crystal X-ray analysis, the basic structural motif of **2** could be determined. Each nickel(II) center is coordinated by four bridging water molecules, generating $Ni(\mu\text{-}OH_2)_2Ni$ diamond chains in the *b* direction (Figure 3a, Table 2). The two other coordination sites are occupied in a *trans* fashion by the *N*-cyano groups of the linear $[Au(CN)_2]^-$ units, thereby yielding a slightly distorted octahedral environment around the nickel(II) center. The closest Au–Au distance, 3.3183(11) Å, indicates the presence of weak aurophilic interactions; viable aurophilic interactions are considered to exist for distances smaller than the sum of the van der Waals radii for gold, 3.6 Å.[20,35]

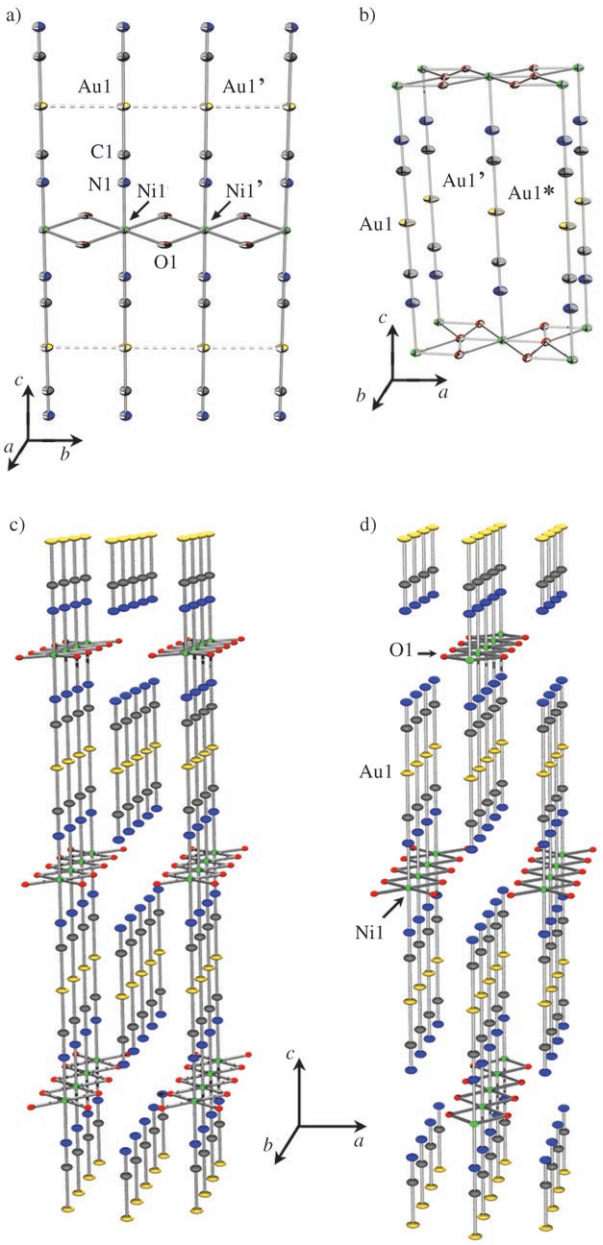

Figure 3. a) Basic structural motif of Ni(μ-OH_2)$_2$[Au(CN)$_2$]$_2$ (**2**). b) Unit cell contents of **2** obtained from initial single-crystal X-ray data analysis, for which all nickel and oxygen atoms have a half-occupancy, hydrogen atoms are omitted for clarity. c) Extended structure of Ni(μ-OH_2)$_2$[Au(CN)$_2$]$_2$ (**2**), after doubling the unit cell along the *c* axis, in the sheet model and d) in the ribbon model. (Ni, green; Au, yellow; C, grey; N, blue.)

The structural model obtained from the initial single-crystal X-ray data generates a random half-occupancy of the nickel and oxygen atoms; Figure 3b shows the contents of one unit cell from the initial single-crystal data analysis. However, some discrepancies can be noticed on comparison of the powder X-ray diffractogram predicted by this model with the one obtained experimentally (Figure 2). A few key observed reflections (e.g., d_{hkl}=4.65 and 6.15 Å) are not predicted by this model. The relative intensities of these reflections are very weak (less than 5%) and, under our experimental conditions for the single-crystal data collection, fall below the 3σ signal-to-noise ratio cutoff used to discriminate between background noise and real signal originating from the sample.

Table 2. Selected bond lengths [Å] and angles [°] for Ni(μ-OH_2)$_2$[Au(CN)$_2$]$_2$ (**2**).[a]

Ni(1)–N(1)	2.0133(5)	Au(1)–Au(1*)	3.5932(12)
Ni(1)–O(1)	2.156(11)	O(1)–H(11)	0.930
Ni(1)–Ni(1′)	3.3183(11)	H(11)···N(11#)	1.788
Au(1)–Au(1′)	3.3183(11)	O(1)–N(11#)	2.709
Ni(1)-O(1)-Ni(1′)	100.6(7)	O(1)-Ni(1)-O(1″)	79.4(7)
O(1)-Ni(1)-N(1)	90.00(2)	O(1)-H(11)-N(11#)	169.8

[a] Symmetry transformations: (′) x, y+1, z; (″) $-x$, $-y$+1, z; (#) x+1/2, y−1/2, z+1/2; (*) $-x$+1/2, $-y$+3/2, $-z$+3/2.

This half-occupancy indicated by the initial single-crystal data analysis could be due to either a truly disordered structure or the existence of a superstructure. The former is discounted on the basis of the additional weak peaks observed in the powder diffractogram. In the latter case, doubling the unit cell along the *c* axis would remove the half occupancy. To maintain the formula unit and charge balance, two of the four nickel sites must then be eliminated, as well as their bound water molecules. To ensure physical feasibility, one site must be removed from each *ab* plane, and the choice of sites eliminated determines the supramolecular arrangement of the basic structural motif: either two-dimensional sheets (Figure 3c) or one-dimensional ribbons (Figure 3d) can be obtained. The powder X-ray diffractograms predicted by using the unit cell with a doubled *c* axis (Table 1) and placement of atoms in the two-dimensional sheet, and one-dimensional ribbon model, respectively, were generated and were compared to the experimental diffractogram obtained for **2** (Figure 2 and Figure S2). The sheet model was rejected due to poor agreement between the predicted and experimental results (Figure S2). On the other hand, the diffractogram simulated for the ribbon model was very similar to the experimental data. All the reflections, including the key weak peaks at d_{hkl}=6.15 and 4.65 Å, are present in both diffractograms and the same relative intensities are observed (Figure 2, inset).

By using the cell information obtained from the powder diffractogram analysis, the single-crystal diffraction data was recollected on the same crystal with the doubled cell. The single-crystal solution that is obtained as a result indeed corresponds to the ribbon model as determined by the powder diffractogram, with no disorder or occupancy issues remaining.

The basic structural motif shown in Figure 3a is still preserved in the ribbon model: Ni(μ-OH_2)$_2$Ni diamond chains are found along the *b* axis, with pendant [Au(CN)$_2$]$^-$ units above and below the chains parallel to the *c* direction. The hydrogen atoms probably lie symmetrically above and below the Ni_2O_2 diamond plane. These ribbons are offset with each other along the *a* and *b* axes and interact through

hydrogen bonds that involve water molecules in one chain, and terminal cyano-nitrogen atoms of the four neighboring chains (Figure S1, Ni–OH···NC, $d_{O-N}=2.709$ Å).

The powder X-ray diffractogram of **1** could be indexed best to a monoclinic cell (Table 1), including the key peaks with a *d* value of 4.65 and 6.15 Å, with dimensions similar to those of **2**. The *b* and *c* axes in **1** are switched with respect to **2**, and the *c*-lattice parameter is doubled relative to the cell obtained for **2** from single-crystal X-ray data analysis. However, it is consistent with the cell for **2** determined from powder X-ray diffraction. Given the nearly isostructural nature of **1** and **2**, $Cu(\mu\text{-}OH_2)_2[Au(CN)_2]_2$ probably adopts the same motif and packing as described for the nickel analogue. The lower symmetry and small differences between the unit cells can be attributed to the Jahn-Teller distorted geometry of the copper(II) center in **1** in contrast to the more-symmetric nickel(II) center in **2**. Attempts to index the powder diffractogram of **1** to the same orthorhombic unit cell failed, as several peaks below 3.1 Å were not predicted.

The axial and equatorial sites of the Jahn-Teller distorted copper(II) centers in **1** were assigned based on the frequencies of the cyanide stretches observed in the infrared spectrum. The *N*-cyano groups in **1** are equatorially bound, as indicated by the strongly blue-shifted 2217 cm^{-1} stretch; axially bound copper(II)-dicyanoaurates show little shift from the 2141 cm^{-1} stretch of free $[Au(CN)_2]^-$ units.[19] The 2171 cm^{-1} stretch is assigned to the pendant side of the $[Au(CN)_2]^-$ unit, which hydrogen bonds to the water molecules, shifting its frequency. Similar assignments can also be made for **2**.

The four water molecules in the copper coordination sphere occupy the remaining equatorial and axial sites, thereby bridging the copper centers in an equatorial-axial fashion. This bridging combination generates an asymmetric diamond chain motif, although accurate Cu–O distances and Cu-O-Cu angles could not be determined. The asymmetric $Cu(\mu\text{-}OH_2)_2Cu$ diamond chains are probably responsible for the reduction in unit cell symmetry, as the chains lie in the *ac* plane, along the *c* direction.

The structural motif adopted by **1** and **2** is unprecedented in cyanometallate chemistry;[11–13] more generally, the aqua-bridged metal chain substructure has not yet, to our knowledge, been observed. Relative to the large number of oxo- and hydroxo-bridged metal centers, only a small number of aqua-bridged copper(II) and nickel(II) dimers are known.[36–38]

If the water is thermally removed, **1** and **2** undergo a significant structural rearrangement to reoccupy some of the vacated metal-coordination sites. The diffractogram of **1a** shows a small number of broad peaks (Figure S3) that are shifted relative to that observed for **1**. Taken together with the large changes in the ν_{CN} frequencies, this suggests that the framework changes upon dehydration. The infrared spectrum of **1a**, which shows one ν_{CN} frequency at 2191 cm^{-1}, may suggest a square-grid structure in which all *N*-cyano groups are equatorially coordinated and equivalent, as observed for related compounds.[18,22,29] We are currently examining these structural changes in more detail.

Magnetic properties of $Cu(\mu\text{-}OH_2)_2[Au(CN)_2]_2$ (1) and $Cu[Au(CN)_2]_2$ (1a): The magnetic susceptibility, χ_M, of **1** and **1a** was measured from 300 to 1.8 K, and their respective effective magnetic moments ($\mu_{eff}=2.828\sqrt{\chi_M T}$) as a function of temperature are shown in Figure 4. The effective magnetic moments observed at 300 K are 1.81 and 1.89 μ_B for **1** and **1a**, respectively, which are typical for isolated copper(II) centers.[39] Below 50 K, as the temperature decreases, the effective magnetic moment for **1** increases, whereas it decreases for the anhydrous **1a**. This suggests the presence of ferro- and antiferromagnetic interactions in **1** and **1a**, respectively. Above 50 K, the inverse of the susceptibility ($1/\chi_M$) for **1** and **1a** can be fitted to a Curie–Weiss law [Eq. (1)]:

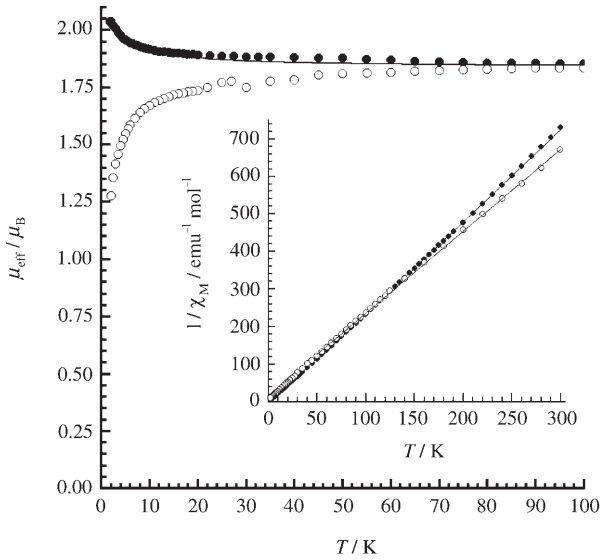

Figure 4. Temperature dependence of the effective magnetic moment (μ_{eff}) of $Cu(\mu\text{-}OH_2)_2[Au(CN)_2]_2$ (**1**) (●) and $Cu[Au(CN)_2]_2$ (**1a**) (○) under a 10 kOe applied field. The solid line represents the best fit to the Baker expression, including a mean field correction. The inset shows the inverse of the susceptibility for **1** (●) and **1a** (○) and the theoretical fits (solid lines) to the Curie–Weiss expression.

$$\chi_M = \frac{Ng^2\mu_B{}^2}{3k_B} \times \frac{S(S+1)}{T-\theta} \quad (1)$$

in which *N* is Avogadro's number, μ_B is the Bohr magneton constant, k_B is the Boltzmann constant, *S* is the total spin value, and θ is the Weiss parameter.[40] For **1**, a value of $\theta=+5.1(3)$ K was obtained ($g=2.084(2)$); the positive θ value is also consistent with ferromagnetic interactions between the $S=1/2$ copper(II) centers in the polymer. For **1a**, fitting to Equation (1) afforded $\theta=-8.2(6)$ K ($g=2.211(4)$). The negative sign of the Weiss parameter reiterates the presence of antiferromagnetic interactions in the anhydrous **1a** polymer.

The magnetic susceptibility of **1** was fitted to the high-temperature series expansion derived by Baker[41] [Eq. (2)] for the regular infinite Heisenberg chain model for $S=1/2$ with the Hamiltonian $H=-J\Sigma_i S_i \times S_{i+1}$:

$$\chi_{\text{chain}} = \frac{Ng^2\mu_B{}^2}{4k_BT} \times \left(\frac{A}{B}\right)^{2/3}$$
$$A = 1.0+5.7979916y+16.902653y^2+29.376885y^3$$
$$+29.832959y^4+14.036918y^5 \qquad (2)$$
$$B = 1.0+2.7979916y+7.0086780y^2+8.653644y^3$$
$$+4.5743114y^4$$

in which $y=J/2k_BT$. This fit yields an exchange coupling constant J of 0.37(2) cm^{-1} and a g value of 2.134(3), consistent with weak ferromagnetic interactions along a chain. To account for interactions present between the chains, a mean field approximation was incorporated into the Baker expression [Eq. (3)]:[40]

$$\chi_{\text{MF}} = \frac{\chi_{\text{chain}}}{1-\chi_{\text{chain}}(2zJ'/Ng^2\mu^2)} \qquad (3)$$

in which z is the number of interacting neighbors. The best fit to Equation (3) afforded a J value of 0.96(5) cm^{-1}, a zJ' value of $-0.58(4)$ cm^{-1}, and a g value of 2.122(2), suggesting weak antiferromagnetic interactions between the chains. However, this result should be treated with caution, as the similar magnitudes of J and zJ' limit the validity of the mean field approximation.[40] Nonetheless, recent theoretical studies linking the ratio of the ordering temperature and the coupling constant (T_N/J) to the J'/J ratio confirms that with the T_N and J values determined for **1**, a J' value of -0.08 cm^{-1} (-0.12 K) should be expected.[42] This is similar to the zJ' value obtained by using Equation (3) with four or six nearest-neighbor chains ($J'=-0.14$ or -0.09 cm^{-1}, respectively), as observed in the structure.

Muon spin-relaxation measurements for Cu(μ-OH$_2$)$_2$[Au(CN)$_2$]$_2$ (1) and Cu[Au(CN)$_2$]$_2$ (1a): To further investigate the magnetic state of **1** at low temperature, zero-field muon spin-relaxation (ZF-μSR) measurements were performed in a ^{3}He/^{4}He dilution refrigerator down to 0.015 K. Figure 5a shows the ZF-μSR asymmetry spectra for Cu(μ-OH$_2$)$_2$[Au(CN)$_2$]$_2$ (**1**) acquired at several temperatures. The asymmetry spectra above 0.20 K were fitted to a "power exponential" relaxation function for the sample signal, such that

$$A(t) \equiv a_0P_z(t) = a_s e^{-(\lambda t)^K} + a_{Ag} \qquad (4)$$

Here, a_s and a_{Ag} are amplitudes reflecting the fraction of muons that stop in the sample and the silver backing plate, respectively. The background signal originates primarily from weak nuclear moments in the silver backing plate, and is both nonrelaxing and temperature independent.[30]

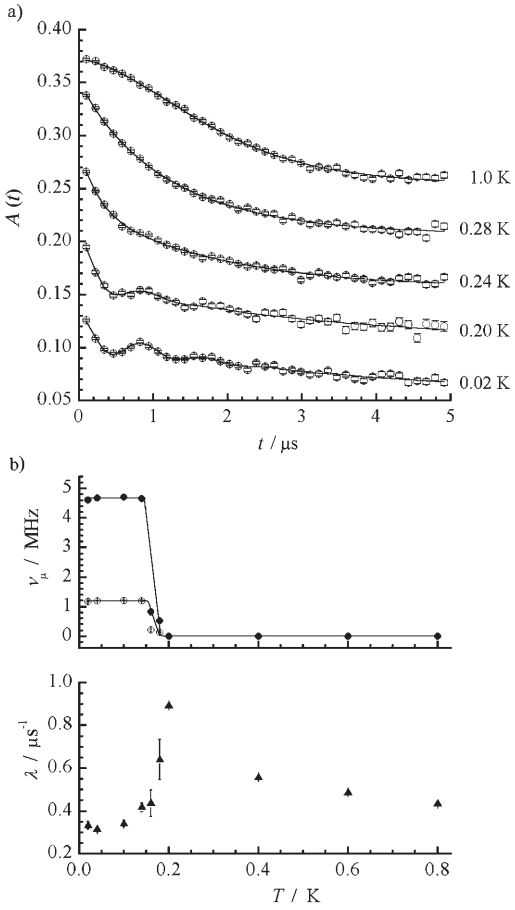

Figure 5. a) ZF asymmetry spectra acquired for Cu(μ-OH$_2$)$_2$[Au(CN)$_2$]$_2$ (**1**) at different temperatures. The solid curves are the fits to Equations (4) and (5). The spectra have been vertically offset from each other for clarity. b) Temperature dependences of the fitted parameters ν_1 (○), ν_2 (●), λ (▲). The solid curves in (b) are simply guides for the eye.

Below 0.20 K, a coherent precession signal is observed, indicating the onset of long-range magnetic order. In the magnetically ordered state, the asymmetry spectra were fitted to the function

$$A(t) \equiv a_0P_z(t) = a_s\left\{\frac{2}{3}[f\cos(2\pi\nu_1 t+\varphi_1)e^{-\Lambda_1 t}+ (1-f)\cos(2\pi\nu_2 t+\varphi_2)e^{-\Lambda_2 t}]+\frac{1}{3}e^{-\lambda t}\right\}+a_{Ag} \qquad (5)$$

For a polycrystalline sample, there is a 1/3 (2/3) probability that the local magnetic field is parallel (transverse) to the muon spin direction. Consequently, only 2/3 of the muon spins precess about the local magnetic field B_μ with frequency $\nu_\mu=\gamma_\mu B_\mu$, for which $\gamma_\mu=0.0852$ $\mu s^{-1}G^{-1}$ is the muon gyromagnetic ratio. In **1**, there are two well-defined muon precession frequencies, ν_1 and ν_2, which correspond to two magnetically nonequivalent muon stopping sites (note: ϕ_1 and ϕ_2 are phase angles). In Equation (5), f is the fraction of muons that senses an average local field $B_1=\gamma_\mu/\nu_1$, and $(1-f)$ is the fraction of muons that senses the average local field $B_2=\gamma_\mu/$

ν_2. The fits to the asymmetry spectra below 0.20 K yielded $f=1/5$. The width of the internal magnetic-field distribution at each muon site is proportional to Λ_1 and Λ_2. The relaxation rate of the 1/3 component is related to the average correlation time, τ_c, and the mean of the square of the fluctuating transverse-field components, $\langle B_T^2\rangle$, by Equation (6)

$$\lambda = \gamma_\mu^2 \langle B_T^2\rangle \frac{\tau_c}{1+(2\pi\nu_\mu\tau_c)^2} \quad (6)$$

in which $\nu_\mu=\gamma_\mu B_{ext}$ is the Larmor frequency of the muon in an external magnetic field B_{ext}. At a spin-freezing phase-transition temperature T_f, the temperature dependence of λ exhibits a cusplike behavior. The critical slowing down of the magnetic fluctuations on approach of T_f from above results in a growth of τ_c, whereas below T_f, the freezing out of the magnetic excitations reduces λ.

The temperature dependences of ν_1, ν_2, and λ are shown in Figure 5b. The maximum in $\lambda(T)$ and the simultaneous increase of ν_1 and ν_2 confirm the existence of a transition to a magnetically ordered state at $T_f\approx0.20$ K.

ZF-μSR measurements were also performed on the anhydrous compound $Cu[Au(CN)_2]_2$ (**1a**). The asymmetry spectra over the entire temperature range were fitted to Equation (4) (Figure 6a). The increase in the relaxation rate λ as temperature decreases (Figure 6b) is consistent with the slowing down of fluctuating Cu spins. However, there is no evidence of magnetic order, that is, there is no oscillatory component as was observed for $Cu(\mu\text{-}OH_2)_2[Au(CN)_2]_2$ (**1**) at low temperatures.

The power K is also plotted in Figure 6b. At 3.2 K, $K\approx1$, as expected for rapidly fluctuating Cu spins.[43] We note that for a single muon stopping site, K is equal to 2 in a dense system of static moments. At low temperatures, K ranges between 1 and 2, suggesting a superposition of field distributions from magnetically inequivalent muon sites. To determine whether the magnetic moments sensed by the muons are static or fluctuating at low temperatures, longitudinal field (LF) μSR measurements were performed on $Cu[Au(CN)_2]_2$ (**1a**). At 0.40 K, a LF of only 100 G was sufficient to completely decouple the muon spin from the local magnetic field and to cause the relaxation of $A(t)$ to vanish. This indicates that the relaxation observed in the ZF asymmetry spectrum at this temperature is due primarily to randomly oriented static copper spins.[43]

Magnetic properties of $Ni(\mu\text{-}OH_2)_2[Au(CN)_2]_2$ (2): The temperature dependence of the magnetic susceptibility (χ_M) for **2** was determined upon cooling with a range of applied external dc magnetic fields (5 Oe to 10 kOe). Selected plots of χ_M as a function of temperature are shown in Figure 7. Above 25 K, the magnetic susceptibility of **2** is field independent and follows the Curie–Weiss expression [Eq. (1)] above 50 K. Fitting the data obtained with an external field of 1 kOe to Equation (1) yielded a θ value of +5.1(2) K ($g=$ 2.256(1)). A field-dependent magnetic behavior is observed below approximately 15 K. Upon exposure to a magnetic

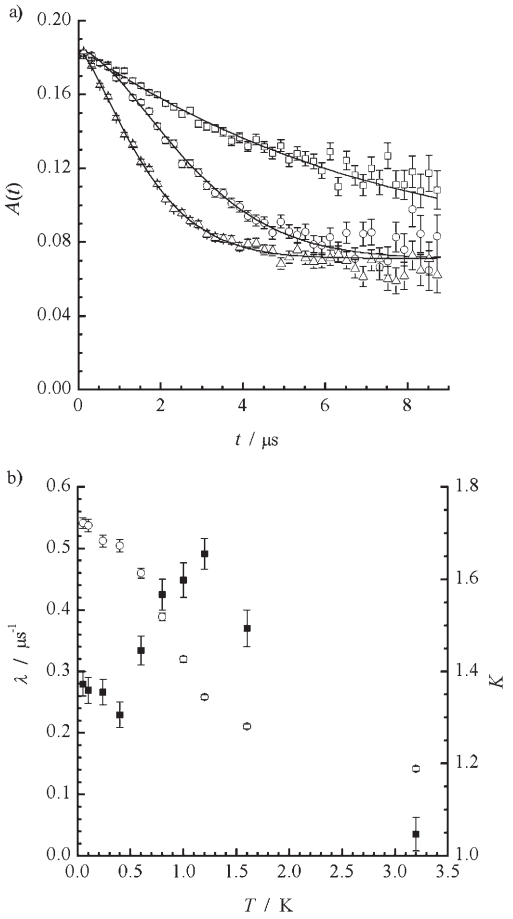

Figure 6. a) ZF asymmetry spectra acquired as a function of temperature for $Cu[Au(CN)_2]_2$ at $T=3.2$ (□), 1.0 (○), 0.05 K (△). The solid curves are fits to Equation (4). b) Temperature dependence of the relaxation rate λ (○) and the power K (■) from the fits.

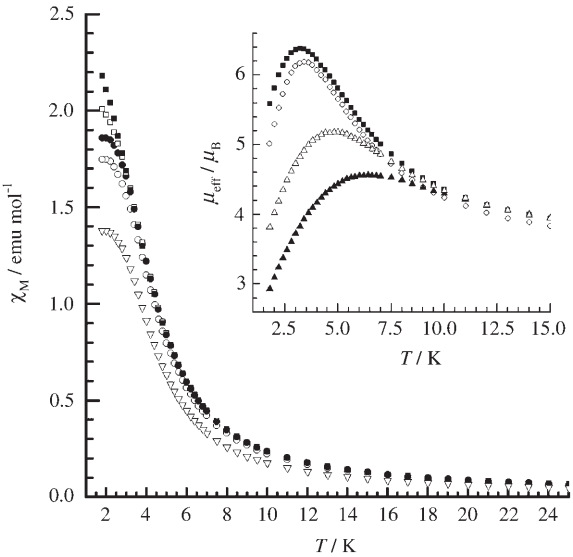

Figure 7. Temperature-dependent magnetic susceptibility (χ_M) of **2** measured in a 1 kOe (■), 500 Oe (□), 250 Oe (●), 50 Oe (○), 10 Oe (▽), 5 kOe (△), 10 kOe (▲) dc field. Inset: effective magnetic moment (μ_{eff}) of **2** in a 50 Oe (○), 1 kOe (■), 5 kOe (△), 10 kOe (▲) dc field.

field of 1 kOe, the magnetic susceptibility increases rapidly below 10 K as the temperature decreases (Figure 7), reaching a value of 2.18 emu mol^{-1} at 1.8 K. If the external magnetic field is smaller than 1 kOe, the magnetic susceptibility still increases below 10 K as the temperature decreases, leveling off at between 2.0 and 1.8 K. The maximum value in susceptibility may correspond to a peak or a plateau, however, the data does not allow discrimination of the two possibilities. Upon application of fields larger than 1 kOe, the overall susceptibility of **2** is lower, due to the more-complete alignment of the spins with the external field.

The inset of Figure 7 shows the effective magnetic moment (μ_{eff}) of **2** as a function of temperature at different magnetic fields. The μ_{eff} observed at 300 K is 3.2 μ_B, as expected for magnetically dilute $S=1$ nickel(II) centers (with a g value of 2.2). A maximum in μ_{eff} is observed at temperatures ranging from 3.4 to 6.4 K, depending on the strength of the external magnetic field. This maximum, occurring at a higher temperature than the maximum in susceptibility (χ_M), indicates that ferromagnetic interactions are also present between the metal centers.

Zero-field cooled (ZFC) and field cooled (FC) magnetization measurements were also conducted on **2** with a dc field ranging from 10 to 800 Oe. No obvious difference was observed between the ZFC and the FC magnetization measurements.

Isothermal magnetization measurements were performed as the applied magnetic field was increased from 0 to 70 kOe at two different temperatures, 1.8 and 10 K (Figure 8 and Figure S4). At 1.8 K, the magnetization curve has a sigmoidal shape: at low fields, the magnetization increases slowly as the applied field is increased, but between 700 and 800 Oe, the magnetization reaches an inflection point, after which it increases more rapidly as the field increases (inset Figure 8). The slope finally decreases above 1 kOe. The magnetization at 1.8 K does not reach saturation over the field-range studied, but tends toward the saturation value expected for a nickel(II) complex (2.2 $N_A\mu_B$ for $g=2.2$). The sigmoidal shape was not observed for measurements performed at higher temperature.

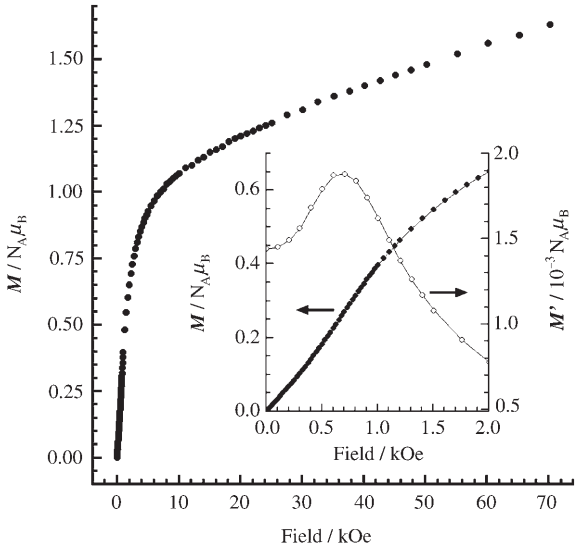

Figure 8. Isothermal magnetization curve of Ni(μ-OH$_2$)$_2$[Au(CN)$_2$]$_2$ at 1.8 K (●). Inset: field dependence of the dc magnetization (***M***, ●) and of the in-phase component of the ac magnetization (***M′***, ○) at 1.8 K, in the low-field region. Lines are guides for the eye.

Measurement of the ac susceptibility of **2** as a function of the applied dc field at 1.8 K (inset Figure 8) gave results consistent with the isothermal dc magnetization measurements performed at the same temperature. This is expected because the in-phase component ***M′*** is a measure of the instantaneous slope d***M***/d***H*** (***M*** being the magnetization) observed in dc experiments. The in-phase component ***M′*** increases to a maximum value at 700 Oe, and then decreases as the field increases, reaching $6.05\times10^{-5}\,N_A\mu_B$ at 25 kOe. The position of the maximum of the in-phase component ***M′*** corresponds to the position of the inflection point of the isothermal dc magnetization curve. The critical field at which a maximum is observed in the in-phase component ***M′*** was determined as a function of temperature up to 3.2 K (Figure 9). As the temperature increases, the maximum shifts to lower field and above 3.2 K, no distinct maximum in the in-phase component could be observed.

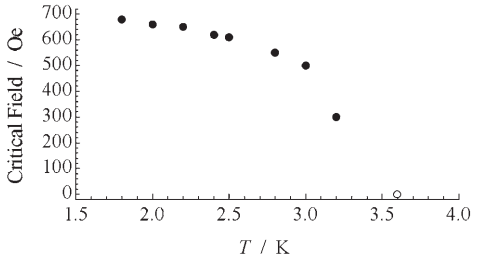

Figure 9. Temperature dependence of the critical field determined from field-dependent ac susceptibility measurements (●). Transition temperature (T_t) at zero-field obtained from μSR experiments (○).

Temperature-dependent ac susceptibility measurements were performed for **2** with an applied ac field of 5 Oe and a driving frequency of 1.00, 10.00, 38.58, 997.34, and 1488.10 Hz. The results are shown in Figure 10. Under zero dc field, a frequency dependence is observed for the in-phase component of the ac susceptibility, χ_M', and a maximum is observed. The position of the maximum shifts to higher temperature (2.16 to 2.42 K) as the frequency is increased from 1.00 to 1488.10 Hz. A frequency-dependent nonzero out-of-phase component of the ac susceptibility, χ_M'', is observed at very low temperature.

Muon spin-relaxation measurements for Ni(μ-OH$_2$)$_2$[Au(CN)$_2$]$_2$ (2): To clarify the nature of the phase transition suggested by the maxima in effective moment (μ_{eff}) and susceptibility (χ_M) observed in the SQUID measurements, ZF-μSR experiments were performed on **2**. The

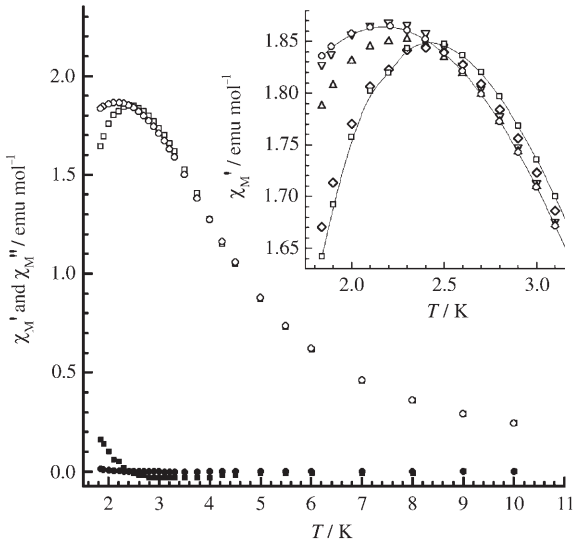

Figure 10. Temperature and frequency dependence of the in-phase (χ_M', empty symbols) and out-of-phase (χ_M'', filled symbols) components of the ac susceptibility of **2** measured under zero dc field and with an ac field of 5 Oe. 1.00 (○), 10.00 (▽), 38.58 (△), 997.34 (◇), 1488.10 Hz (□). Lines are guides for the eye.

ZF-μSR asymmetry spectra for Ni(μ-OH_2)$_2$[Au(CN)$_2$]$_2$ (**2**) (Figure 11a) were best fitted by using the function

$$A(t) \equiv a_0 P_z(t) = a_s\left(\frac{2}{3}e^{-\Lambda t}+\frac{1}{3}e^{-\lambda t}\right)+a_{Ag} \qquad (7)$$

in which the term containing a_s describes the signal originating from muons stopping in the sample, and as before, a_{Ag} is the temperature-independent background signal. This is a similar function to that used in fitting the Cu(μ-OH_2)$_2$[Au(CN)$_2$]$_2$ (**1**) data, although in this case an oscillatory component is not required. There is no indication of long-range magnetic order in Ni(μ-OH_2)$_2$[Au(CN)$_2$]$_2$ (**2**) down to 0.015 K.

Figure 11b shows the temperature dependences of the relaxation rates, Λ and λ, of the 2/3 and 1/3 components, respectively. A spin-freezing transition occurs at $T_f \approx 3.6$ K, as evidenced by the peak in $\lambda(T)$ and the rapid decrease of λ to zero as the temperature falls below 3.6 K. The latter observation, together with the finding that the initial asymmetry of the relaxing signal described by λ does not exceed 1/3, indicates that the frozen spin state is homogeneous.[44] Below T_f, the initial relaxation is so fast that the early part of the signal is not observed, and only the slow-relaxing "1/3 tail" is fully visible. At these temperatures, the relaxation rate Λ is very large, indicating that the distribution of local static fields at the muon sites is extremely broad. All of these observations are consistent with the Ni moments freezing into a state below T_f that resembles a spin-glass.[45]

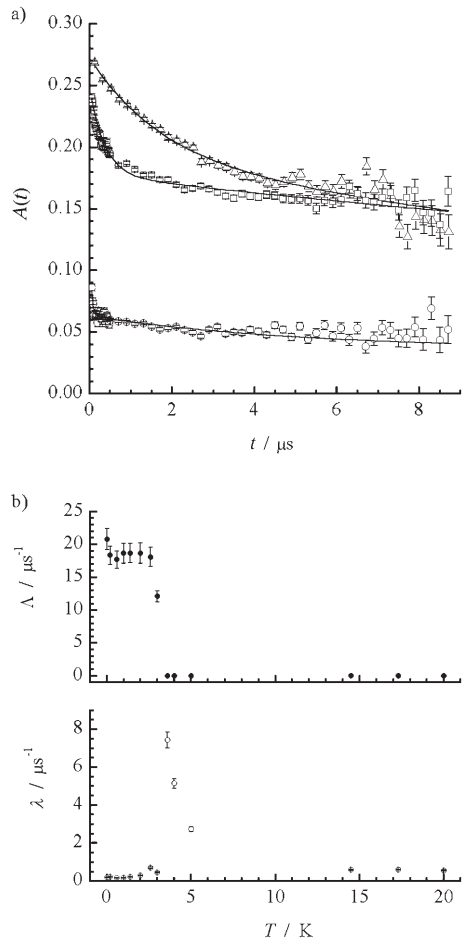

Figure 11. a) ZF asymmetry spectra for Ni(μ-OH_2)$_2$[Au(CN)$_2$]$_2$ at 14.5 (△), 5.0 (□), 0.015 K (○). The solid curves are fits to Equation (7). b) The temperature dependences of the relaxation rates Λ and λ.

Discussion

General magneto-structural correlations: Magnetic exchange between the metal centers in **1** and **2** can occur through several magnetic pathways (Figure 12). The interactions mediated through the short M(μ-OH_2)$_2$M bridges, J_1, are probably the strongest possible interactions in **1** and **2**. The type and strength of interactions mediated by the oxygen atom in such a bridge depends on the extent of overlap between the magnetic orbitals of the metal centers and the orbitals of the oxygen atoms;[40] this, in turn, depends on the structural arrangement.

Other possible magnetic interaction pathways, albeit weaker than J_1 due to the long distances involved, utilize hydrogen-bonding interactions between the [Au(CN)$_2$]$^-$ units and the water molecules, either through M−OH···N···HO−M (J_2) or through M−OH···NCAuCN−M (J_3).[46] Water molecules are known to mediate both ferro- and antiferromagnetic interactions through hydrogen bonding between different spin carriers, including copper(II),[47] nitronylnitroxide radicals,[48] chromium(III),[49] and mixed nickel(II)-radical systems.[50] The [Au(CN)$_2$]$^-$ unit has been observed to medi-

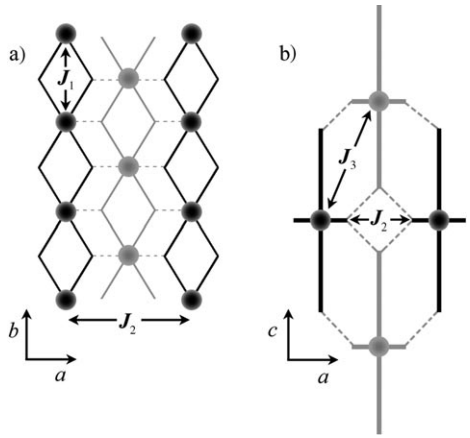

Figure 12. Possible magnetic pathways in **2**: a) interactions along the Ni-(μ-OH_2)$_2$Ni chains (J_1), viewed down the c axis; b) interchain interactions (J_2, J_3), viewed down the chains. Dotted lines indicate hydrogen bonding.

ate magnetic interactions between several first-row transition metals at low temperature.[19,27] A deeper understanding of the magnetic behavior of **1** and **2** can be gained by combining the SQUID magnetometry and ZF-μSR results, and some magneto-structural correlations can be drawn.

Magnetic behavior of Cu(μ-OH_2)$_2$[Au(CN)$_2$]$_2$ (1): According to the structure proposed for **1**, the copper(II) centers are in an axial–equatorial arrangement along the Cu(μ-OH_2)$_2$Cu chain axis. Despite the exhaustive magnetic studies carried out for a range of equatorial–equatorial oxygen-donor-bridged copper(II) dimers,[40,51] which include hydroxo, aqua, acetate, carboxylate, and alkoxo-bridged systems, the magnetic properties of axial-equatorial oxygen-bridged copper(II) dimers have not been investigated in great detail and, given the lack of data, no clear trends have been reported.[37] Naturally, the bond length and angles in the Cu(μ-OH_2)$_2$Cu core play a key role in determining the type and strength of magnetic exchange observed. In general, very weak interactions are mediated through axial-equatorial asymmetric copper(II) bridges, due to poor orbital overlap between the metal center and the bridging atoms occupying the axial positions, and this interaction weakens as axial distance increases. For example, complexes with a Cu–O_{axial} distance between 2.3 and 2.4 Å were found to be ferromagnetic[52] with a coupling constant J smaller than 10 cm^{-1}. In contrast, a larger distance (~2.5 Å) generated a slightly antiferromagnetic complex[53] ($J \sim -0.5$ cm^{-1}). Extended Hückel calculations performed on similar axial-equatorial dichloro-bridged copper(II) systems[54] showed that, for an ideal geometry with 90° angles, no magnetic coupling should exist between the copper(II) centers. Any small ferro- or antiferromagnetic coupling observed for such systems was attributed to structural deviations from ideality.

Thus, the small increase in effective magnetic moment (μ_{eff}) observed for **1** below 20 K (Figure 4) is probably a consequence of weak ferromagnetic interactions occurring between the copper centers through the aqua-bridge (J_1). The positions of the oxygen atoms around the copper centers in **1** could not be refined and, thus, reliable bond lengths and angles involving the oxygen atoms could not be determined. It is, therefore, difficult to put the structural parameters of **1** into context. Nevertheless, the small exchange coupling constant obtained by fitting the data with the Baker expression [Eq. (2)] ($J_{Baker} = J_1 = 0.37(2)$ cm^{-1}) agrees well with the few previously reported values for axial-equatorial oxygen-bridged copper(II) systems.[52]

Interactions between the ferromagnetically coupled chains through hydrogen bonding become more important at very low temperatures and yield a long-range magnetically ordered state below 0.20 K, as detected by the ZF-μSR experiments (Figure 5); observation of a three-dimensionally ordered system implies that the magnetic interactions through the long J_2 and J_3 pathways must be non-negligible. It also suggests that magnetic exchange along J_2 must be ferromagnetic, as antiferromagnetic interactions along J_2 would lead to a frustrated system, irrelevant of the sign of J_3 (see below). The overall long-range order in **1** could be either ferromagnetic or antiferromagnetic, depending on the type of magnetic exchange along J_3, although the negative zJ' coupling constant determined [Eq. (3)] is consistent with antiferromagnetic ordering.

Magnetic behavior of Ni(μ-OH_2)$_2$[Au(CN)$_2$]$_2$ (2): Despite their very similar structures, the magnetic behavior of Ni(μ-OH_2)$_2$[Au(CN)$_2$]$_2$ (**2**) was found to differ from that of the copper analogue (**1**). The increase in μ_{eff} as temperature decreases to a maximum between 3 and 5 K observed by SQUID magnetometry (inset Figure 7) suggests the presence of ferromagnetic interactions in **2**. Similar to **1**, these ferromagnetic interactions are probably mediated through the Ni(μ-OH_2)$_2$Ni bridge (J_1). Very few aqua-bridged nickel(II) dimers or chains have been reported,[38,55] and of these, the magnetic properties were rarely investigated. Antiferromagnetic interactions were observed in the double-stranded chain [Ni_2(Hpdc)$_2$(μ-H_2O)$_2$(H_2O)$_2$] (H_3pdc = 3,5-pyrazoledicarboxylic acid), in which water molecules link two [Ni(Hdcp)] chains together, with Ni–O bond lengths of 2.075(2) and 2.145(2) Å and a Ni-O-Ni angle of 100.94(9)°.[38] The double aqua-bridge was determined to be the dominant magnetic pathway in this system, yielding a J value of $-1.6(2)$ cm^{-1}. The absence of further examples limits the discussion of any general magnetostructural correlations regarding Ni(μ-OH_2)$_2$Ni units.

With a small external field, maxima/plateaus in the susceptibility (χ_M) observed below 2 K (Figure 7) indicate that, at low temperatures, the ferromagnetically coupled chains interact with each other through hydrogen-bond-mediated interactions (either J_2 or J_3). Either antiferromagnetic interactions or a spin-glass type behavior is consistent with this experimental data. However, if the external field is greater than 1 kOe, these weak interchain interactions are overcome, and the chains align with the field. The combination of ferro- and antiferromagnetic interactions/spin-glass behavior in **2** is also apparent in the sigmoidal shape of the iso-

thermal magnetization curve at 1.8 K. The critical magnetic field at 1.8 K was determined to be 700 Oe from both the inflection point in the dc and the maximum in the ac isothermal magnetization curves (Figure 8). As the temperature increases, the critical field decreases, because it becomes easier to align the chains with the external field.

This type of magnetic behavior is similar to that of a metamagnetic system.[39,56] Such systems are commonly composed of ferro- or ferrimagnetic sheets or chains that interact or order antiferromagnetically at low temperature and field, but undergo a transition to a ferromagnetic state at a critical field. Examples of metamagnetic coordination polymers include monometallic azido–nickel(II),[57] iron(II),[58] malonato–copper(II)[59] systems as well as a range of bimetallic or metal-radical systems.[60] However, metamagnet type transitions have not, to our knowledge, been reported in the case of the zero-field state being a spin-glass.

To clarify the nature of the magnetic state of **2** under zero-field, that is, whether antiferromagnetic ordering or spin-glass behavior is operative, the results of the ZF-μSR experiments were invaluable. Indeed, the asymmetry spectra of **2** indicate that no long-range order is present in **2** in zero external field (Figure 11), however, the results are characteristic of a transition to a spin-glass state at 3.6 K. The presence of an out-of-phase signal and the frequency dependence of both phase components in the ac susceptibility (Figure 10) also support the formation of a spin-glass system, although no difference could be observed between the ZFC and FC magnetization measurements. This can be attributed to the fact that the glass transition temperature approaches the temperature limit of the SQUID magnetometer. The formation of a spin-glass generally requires an element of spin frustration from competing magnetic interactions. A negative coupling constant J_2 (Figure 12) would naturally lead to spin frustration if J_3 has a significant nonzero value, either positive or negative.

Comparison of magnetic behaviors: The differences between the magnetic behavior observed for compounds **1** and **2** probably arise from 1) the Jahn-Teller distorted geometry of the copper(II) centers in **1** and 2) the extra unpaired electron on the nickel(II) centers in **2**. Thus, the Jahn-Teller bond lengthening in **1** effectively weakens all three magnetic interactions pathways, leading to a magnetic phase-transition one order-of-magnitude lower than the nickel analogue. Both systems show ferromagnetic interactions along the M-(μ-OH_2)$_2$M chain, implying that the magnetic orbitals are orthogonal in this direction.[40] However, the sign of the key J_2 pathway is predicted to be positive in **1** and negative in **2**; the extra magnetic orbital in nickel(II) appears to provide an overlap that yields interchain antiferromagnetic interactions.

Conclusion

A new basic structural motif among cyanometallate-based coordination polymers was identified in the two nearly isostructural M(μ-OH_2)$_2$[$Au(CN)_2$]$_2$ (M = Cu (**1**), Ni (**2**)) coordination polymers. The central M(μ-OH_2)$_2$M aqua-bridged chain motif is a surprisingly rare structural feature, and should serve as a new "point of reference" for further modification and research. The metal centers are ferromagnetically coupled along the chains in both compounds. Through interchain interactions involving hydrogen bonding and the [$Au(CN)_2$]$^-$ units, the chains magnetically order in **1** and form a spin-glass in **2** at low temperature. This study also illustrates the importance of weak interactions and their power to impact magnetic properties.

Experimental Section

General procedures and characterizations: All manipulations were performed under ambient conditions. All reagents were purchased and were used as received. Cu(H_2O)$_2$[$Au(CN)_2$]$_2$ (**1**) and Cu[$Au(CN)_2$]$_2$ (**1a**) were prepared as previously described.[29] Infrared spectra were recorded by using a Thermo Nicolet Nexus 670 FTIR spectrometer. Samples were prepared as KBr pressed pellets. Microanalyses (C, H, N) were performed by Mr. Miki Yang at Simon Fraser University. Thermogravimetric analysis (TGA) data were collected under ambient atmosphere by using a Shimadzu TGA-50 instrument.

Synthesis of Ni(H_2O)$_2$[$Au(CN)_2$]$_2$ (2): $Ni(NO_3)_2 \cdot 6H_2O$ (0.291 g, 1.00 mmol) was dissolved in water (2 mL) and an aqueous solution (2 mL) of K[$Au(CN)_2$] (0.575 g, 1.99 mmol) was added dropwise. A pale blue-green precipitate of Ni(H_2O)$_2$[$Au(CN)_2$]$_2$ (**2**) was formed within several seconds, collected by filtration, and air-dried. The composition of the precipitate was confirmed by conducting elemental analysis and TGA. Yield 0.433 g (73%). IR (KBr): $\tilde{\nu}$ = 3416 (br), 3116 (br), 3033 (br), 2214 (s), 2204 (sh), 2170 (s), 1537 (m), 910 (m), 756 cm^{-1} (w); elemental analysis calcd (%) for $C_4H_4N_4Au_2NiO_2$: C 8.11, H 0.68, N 9.45; found: C 8.31, H 0.74, N 9.20. Care must be taken during the synthesis of **2** as blue K$Ni[Au(CN)_2]_3$ can be obtained as a side product if a slight excess of K[$Au(CN)_2$] is used, if the precipitate is left in solution for several days, or if the reaction is very concentrated.[61] The purity of **2** can be determined by powder X-ray diffraction.

X-ray crystallographic analysis: Crystallographic data are listed in Table 1 and Table S1. Powder X-ray diffraction data for **1** and **1a** were collected by using a RINT2000 diffractometer equipped with a Cu rotating-anode source (50 kV and 100 mA) and a scintillation-counter detector. Samples were mounted in a tube and irradiated in a scan step of 0.02° at a scan speed of 10° min^{-1}. Data was measured between 4 and 135° in 2θ. Powder X-ray diffraction data for **2** was collected by using a Bruker D8 Advance diffractometer equipped with a Cu sealed-tube source (powered at 40 kV and 40 mA), a graphite monochromator, and a scintillation detector. Data was collected from 3 to 70° in 2θ by using a step of 0.02° and a total counting time of 1.5 s per step. To obtain a higher-quality diffractogram in the 13 to 21° range, data was also collected with a total counting time of 130 s per step (same step size).

Indexing of the powder diffractograms of **1** and **2** was performed by using *Win*PLOTR.[62] The simulation of powder diffractograms from atomic coordinates and comparison with experimentally obtained powder diffractograms were conducted by using POWDER CELL.[63]

Poor-quality pale blue-green crystals of **2** were obtained by recrystallization under hydrothermal conditions, in which 50 mg of **2** were sealed in a 5 mL pyrex ampoule with 3 mL of water. The ampoule was heated to 125 °C for 6 h in a hydrothermal vessel and was then cooled down to

100 °C at 0.5 °C h^{-1}, held at that temperature for 12 h, and then cooled to RT at 1 °C h^{-1}.

A crystal of **2** suitable for single-crystal X-ray diffraction study was mounted on a glass fiber by using epoxy adhesive. Single-crystal X-ray diffraction data in the range $4° < 2\theta < 60°$ were collected by using an Enraf Nonius CAD4F diffractometer equipped with a $Mo_{K\alpha}$ source, controlled by using the DIFRAC program.[64] Diffraction peaks were very broad, consistent with poor crystal quality. The NRCVAX Crystal Structure System was used to perform data reduction, including Lorentz and polarization corrections.[65] The structure was determined by using CRYSTALS;[66] it was solved by using the Sir 92 routine and was expanded by using Fourier techniques. The Au and Ni atoms were refined with anisotropic thermal parameters, whereas the C, N, and O atoms were refined with isotropic thermal parameters. The hydrogen atom was geometrically placed and its position and isotropic thermal parameter were not refined. Full matrix least-squares refinement (217 unique reflections included) on F (14 parameters) converged to $R_1 = 0.0370$, $wR_2 = 0.0376$, and GOF = 1.0503 [$I_o > 2.5\sigma(I_o)$]. Diagrams were obtained by using Ortep-3 (version 1.076)[67] and POV-Ray (version 3.6.0).[68]

CCDC 600062 contains the supplementary crystallographic data for this paper. These data can be obtained free of charge from the Cambridge Crystallographic Data Center via www.ccdc.cam.ac.uk/data_request/cif.

Magnetic measurements by SQUID magnetometry: Magnetization measurements were performed by using a Quantum Design MPMS-XL-7S SQUID magnetometer equipped with an Evercool liquid-helium dewar. Microcrystalline samples of **1** and **2** were packed into gelatin capsules and were mounted in diamagnetic plastic straws, whereas sample **1a** was packed into a cylindrical, airtight PVC sample holder.[69] All data were corrected for the diamagnetism of the constituent atoms by using Pascal's constants and data for **1a** were corrected for the signal of the sample holder.[40]

Direct current (dc) magnetization of compounds **1**, **1a**, and **2** was measured upon cooling from 300 to 1.8 K under an externally applied dc field of 10 kOe. In addition, the temperature-dependent magnetization of **1** and **2** was recorded under different fields (100 Oe for **1** and 50, 250, 500, 750, and 1 kOe for **2**). Zero-field cooled (ZFC) and field cooled (FC) magnetization measurements were performed for **2** with fields of 10, 100, and 800 Oe. The magnetization of **2** as a function of dc field strength (from 0 to 70 kOe) was recorded at several temperatures (2.0, 2.5, 3.0, 3.5, 4, and 10 K); in each case, the sample was first cooled from 100 K under zero-applied field.

Alternating current (ac) susceptibility measurements in zero-applied dc field were performed for **2** as a function of temperature (between 1.8 and 50 K) and operating frequency (1.00, 10.00, 38.58, 997.34, and 1488.10 Hz). The amplitude of the ac field was fixed at 5 Oe. The isothermal ac susceptibility of **2** as a function of the applied dc field, from 0 to 70 kOe, was also measured at several temperatures (1.8, 2.0, 2.2, 2.4, 2.5, 2.8, 3.0, 3.2, and 3.5 K), with an ac field of 5 Oe and a driving frequency of 997.34 Hz.

Muon spin-relaxation (μSR) measurements: The μSR experiments were performed on the M15 surface muon channel at the TRI-University Meson Facility (TRIUMF) in Vancouver, Canada. For each compound (**1**, **1a**, and **2**), two pressed 1-cm diameter polycrystalline pellets with masses from 250 to 500 mg were prepared and varnished onto a silver backing plate, which was thermally anchored to the cold finger of a dilution refrigerator. Figure 13 shows the arrangement of scintillation detectors used in the experiment. The initial polarization, $P_z(0)$, was directed antiparallel to the beam momentum p_μ (i.e., along the z axis). The μSR measurements were taken both in zero external magnetic field (ZF), and in a longitudinal field (LF) geometry with the magnetic field applied parallel to $P_z(0)$.

A counter placed upstream of the sample was used to detect an incoming positive muon (μ^+) and to establish time $t = 0$. The muons were implanted into the sample, where they subsequently decayed to a positron and two neutrinos. The forward (F) and backward (B) detectors sensed the decay positrons. The time-differential histogram rate, $N(t)$, for each positron detector is described by the continuous function

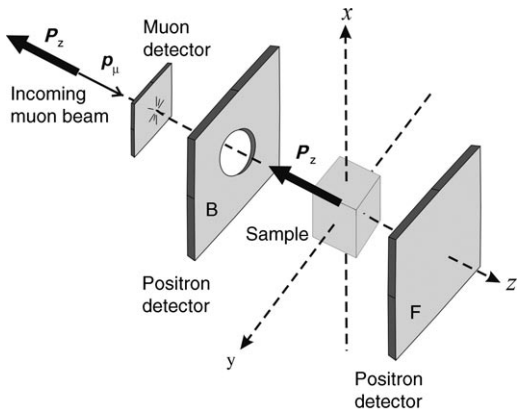

Figure 13. Schematic of the experimental geometry used to carry out the μSR measurements. The incoming muon beam has a spin polarization of nearly 100 % along the beam direction.

$$N_{B,F}(t) = N_0^{B,F} e^{-t/\tau_\mu}[1 \pm a_{B,F} P_z(t)] + B_{B,F} \quad (8)$$

Here, $N_0^{B,F}$ is the count rate at $t = 0$, $\tau_\mu = 2.197$ μs is the mean muon lifetime, $a_{B,F}$ is the intrinsic asymmetry of each positron detector, and $B_{B,F}$ is a time-independent background. The ratio $\alpha = N_0^F/N_0^B$ was determined by fitting the raw time spectra. After subtracting the experimentally determined random backgrounds $B_{B,F}$ from Equation (8), the μSR "asymmetry" spectrum was formed as follows

$$A(t) = a_0 P_z(t) = \frac{N_B(t) - N_F(t)}{N_B(t) + N_F(t)} \quad (9)$$

in which $a_B = a_F \equiv a_0$. Note that this isolates the desired information, which is the time evolution of the muon spin polarization, $P_z(t)$.

Acknowledgements

This work was supported by FQRNT of Québec (J.L.), NSERC, TRIUMF, and the World Gold Council GROW Program. The SQUID magnetometer facility was funded by CFI and BCKDF. The authors thank Profs. Robert C. Thompson (University of British Columbia), Fred W.B. Einstein, and Dr. Raymond J. Batchelor (Simon Fraser University) for useful discussions, Prof. Ken Sakai (Kyushu) for measuring the powder diffraction data for **1** and **1a**, and Dr. Brian O. Patrick (University of British Columbia) for measuring the powder diffraction data for **2**.

[1] a) C. Janiak, *Dalton Trans.* **2003**, 2781–2804; b) S. Decurtins, R. Pellaux, G. Antorrena, F. Palacio, *Coord. Chem. Rev.* **1999**, *190–192*, 841–854; c) J. L. Stuart, *Chem. Soc. Rev.* **2003**, *32*, 276–288.

[2] M. Verdaguer, A. Bleuzen, V. Marvaud, J. Vaissermann, M. Seuleiman, C. Desplanches, A. Scuiller, C. Train, R. Garde, G. Gelly, C. Lomenech, I. Rosenman, P. Veillet, C. Cartier, F. Villain, *Coord. Chem. Rev.* **1999**, *190–192*, 1023–1047.

[3] a) S. Kitagawa, R. Kitaura, S.-I. Noro, *Angew. Chem.* **2004**, *116*, 2388–2430; *Angew. Chem. Int. Ed.* **2004**, *43*, 2334–2375; b) B. Kesanli, W. Lin, *Coord. Chem. Rev.* **2003**, *246*, 305–326; c) O. M. Yaghi, M. O'Keeffe, N. W. Ockwig, H. K. Chae, M. Eddaoudi, J. Kim, *Nature* **2003**, *423*, 705–714.

[4] Anonymous, *Miscellanea Berolinensia ad Incrementum Scientiarum (Berlin)* **1710**, *1*, 377.

[5] J. F. Keggin, F. D. Miles, *Nature* **1936**, *137*, 577.

[6] H. J. Buser, A. Ludi, W. Petter, Schwarzenbach, *J. Chem. Soc. Chem. Commun.* **1972**, 1299.

[7] F. Herren, P. Fisher, A. Ludi, W. Hälg, *Inorg. Chem.* **1980**, *19*, 956–959.
[8] a) J. S. Miller, *MRS Bull.* **2000**, *25*, 60–64; b) M. Ohba, H. Okawa, *Coord. Chem. Rev.* **2000**, *198*, 313–328; c) S. M. Holmes, G. S. Girolami, *J. Am. Chem. Soc.* **1999**, *121*, 5593–5594; d) E. Ruiz, A. Rodriguez-Fortea, S. Alvarez, M. Verdaguer, *Chem. Eur. J.* **2005**, *11*, 2135–2144.
[9] a) S. S. Kaye, J. R. Long, *J. Am. Chem. Soc.* **2005**, *127*, 6506–6507; b) K. W. Chapman, P. D. Southon, C. L. Weeks, C. Kepert, *Chem. Commun.* **2005**, 3322–3323.
[10] L. G. Beauvais, M. P. Shores, J. R. Long, *J. Am. Chem. Soc.* **2000**, *122*, 2763–2772.
[11] K. R. Dunbar, R. A. Heintz, *Prog. Inorg. Chem.* **1997**, *45*, 283–391.
[12] J. Lefebvre, D. B. Leznoff in *Macromolecules Containing Metal and Metal-Like Elements*, *Vol. 5* (Eds.: A. S. Abd-El-Aziz, C. E. Carraher, Jr., C. U. Pittman, Jr., M. Zeldin), Wiley-Interscience, **2005**, pp. 155–208.
[13] T. Iwamoto in *Comprehensive Supramolecular Chemistry, Vol. 6* (Eds.: J. M. Lehn, J. L. Atwood, J. E. D. Davies, D. D. MacNicol, F. Vogtle, G. T. B. Alberti), Pergamon, **1996**, p. 643.
[14] a) J. H. Rayner, H. M. Powell, *J. Chem. Soc.* **1952**, 319–328; b) T. Iwamoto, S. Nishikiori, Y. A. Dyadin, D. V. Soldatov, *J. Struct. Chem.* **1999**, *40*, 750–756; c) T. Iwamoto in *Inclusion Compounds, Vol. 5* (Eds.: J. L. Atwood, J. E. D. Davies, D. D. MacNicol), Oxford University Press, London, **1991**, p. 177.
[15] B. F. Hoskins, R. Robson, *J. Am. Chem. Soc.* **1990**, *112*, 1546–1554.
[16] a) O. Kahn, J. Larionova, L. Ouahab, *Chem. Commun.* **1999**, 945–952; b) J. Larionova, J. Sanchiz, S. Golhen, L. Ouahab, O. Kahn, *Chem. Commun.* **1998**, 953–954; c) J. Larionova, R. Clérac, J. Sanchiz, O. Kahn, S. Golhen, L. Ouahab, *J. Am. Chem. Soc.* **1998**, *120*, 13088–13095; d) W. Dong, Y.-Q. Sun, L.-N. Zhu, D.-Z. Liao, Z.-H. Jiang, S.-P. Yan, P. Cheng, *New J. Chem.* **2003**, *27*, 1760–1764; e) S. Willemin, J. Larionova, R. Clerac, B. Donnadieu, B. Henner, X. F. Le Goff, C. Guerin, *Eur. J. Inorg. Chem.* **2003**, 1866–1872.
[17] D. B. Leznoff, J. Lefebvre, *Gold Bull.* **2005**, *38*, 47–54.
[18] E. Colacio, F. Lloret, R. Kivekaes, J. Ruiz, J. Suarez-Varela, M. R. Sundberg, *Chem. Commun.* **2002**, 592–593.
[19] D. B. Leznoff, B.-Y. Xue, R. J. Batchelor, F. W. B. Einstein, B. O. Patrick, *Inorg. Chem.* **2001**, *40*, 6026–6034.
[20] H. Schmidbaur, *Chem. Soc. Rev.* **1995**, *24*, 391–400, and references therein.
[21] a) M. A. Rawashdeh-Omary, M. A. Omary, H. H. Patterson, J. P. Fackler, Jr., *J. Am. Chem. Soc.* **2001**, *123*, 11237–11247; b) M. A. Rawashdeh-Omary, M. A. Omary, H. H. Patterson, *J. Am. Chem. Soc.* **2000**, *122*, 10371–10380.
[22] W. Dong, L.-N. Zhu, Y.-Q. Sun, M. Liang, Z.-Q. Liu, D.-Z. Liao, Z.-H. Jiang, S.-P. Yan, P. Cheng, *Chem. Commun.* **2003**, 2544–2545.
[23] S. C. Abrahams, J. L. Bernstein, R. Liminga, *J. Chem. Phys.* **1980**, *73*, 4585–4590.
[24] S. C. Abrahams, L. E. Zyontz, J. L. Bernstein, *J. Chem. Phys.* **1982**, *76*, 5458–5462.
[25] B. F. Hoskins, R. Robson, N. V. Y. Scarlett, *Angew. Chem.* **1995**, *107*, 1317–1318; *Angew. Chem. Int. Ed. Engl.* **1995**, *34*, 1203–1204.
[26] a) A. Stier, K.-J. Range, *Z. Naturforsch. B* **1996**, *51*, 698–702; b) J. C. F. Colis, C. Larochelle, R. Staples, R. Herbst-Irmer, H. Patterson, *Dalton Trans.* **2005**, 675–679.
[27] D. B. Leznoff, B.-Y. Xue, B. O. Patrick, V. Sanchez, R. C. Thompson, *Chem. Commun.* **2001**, 259–260.
[28] a) D. B. Leznoff, B. Y. Xue, C. L. Stevens, A. Storr, R. C. Thompson, B. O. Patrick, *Polyhedron* **2001**, *20*, 1247–1254; b) N. D. Draper, R. J. Batchelor, B. C. Sih, Z.-G. Ye, D. B. Leznoff, *Chem. Mater.* **2003**, *15*, 1612–1616; c) C. J. Shorrock, B.-Y. Xue, P. B. Kim, R. J. Batchelor, B. O. Patrick, D. B. Leznoff, *Inorg. Chem.* **2002**, *41*, 6743–6753; d) D. B. Leznoff, N. D. Draper, R. J. Batchelor, *Polyhedron* **2003**, *22*, 1735–1743; e) N. D. Draper, R. J. Batchelor, D. B. Leznoff, *Cryst. Growth Des.* **2004**, *4*, 621–632; f) N. D. Draper, R. J. Batchelor, P. M. Aguiar, S. Kroeker, D. B. Leznoff, *Inorg. Chem.* **2004**, *43*, 6557–6567.
[29] J. Lefebvre, R. J. Batchelor, D. B. Leznoff, *J. Am. Chem. Soc.* **2004**, *126*, 16117–16125.
[30] A. Schenck, *Muon Spin Rotation Spectroscopy: Principles and Applications in Solid State Physics*, Hilger, Bristol, England, **1985**.
[31] a) T. Lancaster, S. J. Blundell, F. L. Pratt, M. L. Brooks, J. L. Manson, E. K. Brechin, C. Cadiou, D. Low, E. J. L. McInnes, R. E. P. Winpenny, *J. Phys. Condens. Matter* **2004**, *16*, S4563–S4582; b) J. L. Manson, T. Lancaster, L. C. Chapon, S. J. Blundell, J. A. Schlueter, M. L. Brooks, F. L. Pratt, L. C. Nygren, J. S. Qualls, *Inorg. Chem.* **2005**, *44*, 989–995; c) T. Lancaster, S. J. Blundell, F. L. Pratt, E. Coronado, J. R. Galan-Mascaros, *J. Mater. Chem.* **2004**, *14*, 1518–1520.
[32] T. Jestädt, M. Kurmoo, S. J. Blundell, F. L. Pratt, C. J. Kepert, K. Prassides, B. W. Lovett, I. M. Marshall, A. Husmann, K. H. Chow, R. M. Valladares, C. M. Brown, A. Lappas, *J. Phys. Condens. Matter* **2001**, *13*, 2263–2270.
[33] G. Maruta, K. Nishiyama, S. Takeda, *Polyhedron* **2001**, *20*, 1185–1188.
[34] W.-F. Yeung, W.-T. Wong, J.-L. Zuo, T.-C. Lau, *J. Chem. Soc. Dalton Trans.* **2000**, 629–631.
[35] a) P. Pyykkö, *Angew. Chem.* **2004**, *116*, 4512–4557; *Angew. Chem. Int. Ed.* **2004**, *43*, 4412–4456, and references therein; b) M. Bardaji, A. Laguna, *J. Chem. Educ.* **1999**, *76*, 201–203.
[36] a) H. O. Davies, R. D. Gillard, M. B. Hursthouse, A. Lehmann, *J. Chem. Soc. Chem. Commun.* **1993**, 1137–1139; b) E. Dubler, G. Hänggi, H. Schmalle, *Inorg. Chem.* **1990**, *29*, 2518–2523; c) O. Svajlenova, J. Vanco, J. Marek, *Acta Crystallogr. Sect. C* **2004**, *C60*, m275–m277; d) P. J. van Koningsbruggen, J. W. van Hal, E. Müller, R. A. G. de Graaff, *J. Chem. Soc. Dalton Trans.* **1993**, 1371–1375.
[37] D. Ghoshal, T. K. Maji, G. Mostafa, S. Sain, T.-H. Lu, J. Ribas, E. Zangrando, N. R. Chaudhuri, *Dalton Trans.* **2004**, 1687–1695.
[38] P. King, R. Clérac, C. E. Anson, A. K. Powell, *Dalton Trans.* **2004**, 852–861.
[39] R. L. Carlin, *Magnetochemistry*, Springer, **1986**.
[40] O. Kahn, *Molecular Magnetism*, VCH, Weinheim, **1993**.
[41] G. A. Baker, G. S. Rushbrooke, H. E. Gilbert, *Phys. Rev.* **1964**, *135*, A1272–A1277.
[42] C. Yasuda, S. Todo, K. Hukushima, F. Alet, M. Keller, M. Troyer, H. Takayama, *Phys. Rev. Lett.* **2005**, *94*, 217201.
[43] R. S. Hayano, Y. J. Uemura, J. Imazato, N. Nishida, T. Yamazaki, R. Kubo, *Phys. Rev. B* **1979**, *20*, 850–859.
[44] G. M. Kalvius, D. R. Noakes, O. Hartmann in *Handbook on the Physics and Chemistry of Rare Earths, Vol. 32* (Eds.: K. A. Gschneidner, L. Eyring, G. H. Lander), Elsevier, **2001**, p. 55.
[45] Y. J. Uemura, T. Yamazaki, D. R. Harshmann, M. Senba, E. J. Ansaldo, *Phys. Rev. B* **1985**, *31*, 546–563.
[46] C. Desplanches, E. Ruiz, A. Rodriguez-Fortea, S. Alvarez, *J. Am. Chem. Soc.* **2002**, *124*, 5197–5205.
[47] W. Plass, A. Pohlmann, J. Rautengarten, *Angew. Chem.* **2001**, *113*, 4333–4336; *Angew. Chem. Int. Ed.* **2001**, *40*, 4207–4210.
[48] C. Rancurel, N. Daro, O. Benedi Borobia, E. Herdtweck, J.-P. Sutter, *Eur. J. Org. Chem.* **2003**, 167–171.
[49] M. Ardon, A. Bino, K. Michelsen, E. Pedersen, R. C. Thompson, *Inorg. Chem.* **1997**, *36*, 4147–4150.
[50] D. Luneau, P. Rey, J. Laugier, E. Belorizky, A. Cogne, *Inorg. Chem.* **1992**, *31*, 3578–3584.
[51] G. V. R. Chandramouli, T. K. Kundu, P. T. Manoharan, *Aust. J. Chem.* **2003**, *56*, 1239–1248.
[52] a) S. Sain, T. K. Maji, G. Mostafa, T.-H. Lu, J. Ribas, X. Tercero, N. R. Chaudhuri, *Polyhedron* **2003**, *22*, 625–631; b) G. A. van Albada, I. Mutikainen, O. Roubeau, U. Turpeinen, J. Reedijk, *Inorg. Chim. Acta* **2002**, *331*, 208–215.
[53] J.-P. Costes, F. Dahan, J.-P. Laurent, *Inorg. Chem.* **1985**, *24*, 1018–1022.
[54] a) M. Rodriguez, A. Llobet, M. Corbella, *Polyhedron* **2000**, *19*, 2483–2491; b) M. Rodriguez, A. Llobet, M. Corbella, A. E. Martell, J. Reibenspies, *Inorg. Chem.* **1999**, *38*, 2328–2334, and references therein.
[55] a) D. Lee, P.-L. Hung, B. Spingler, S. J. Lippard, *Inorg. Chem.* **2002**, *41*, 521–531; b) A. M. Barrios, S. J. Lippard, *J. Am. Chem. Soc.*

2000, *122*, 9172–9177; c) A. M. Barrios, S. J. Lippard, *J. Am. Chem. Soc.* **1999**, *121*, 11751–11757; d) F. A. Cotton, B. H. C. Winquist, *Inorg. Chem.* **1969**, *8*, 1304–1312.
[56] J. S. Miller, A. J. Epstein, *Angew. Chem.* **1994**, *106*, 399–432; *Angew. Chem. Int. Ed. Engl.* **1994**, *33*, 385–415.
[57] a) P. S. Mukherjee, S. Dalai, E. Zangrando, F. Lloret, N. R. Chaudhuri, *Chem. Commun.* **2001**, 1444–1445; b) M. Monfort, I. Resino, J. Ribas, H. Stoeckli-Evans, *Angew. Chem.* **2000**, *112*, 197–199; *Angew. Chem. Int. Ed.* **2000**, *39*, 191–193.
[58] X. Hao, Y. Wei, S. Zhang, *Chem. Commun.* **2000**, 2271–2272.
[59] T.-F. Liu, H.-L. Sun, S. Gao, S.-W. Zhang, T.-C. Lau, *Inorg. Chem.* **2003**, *42*, 4792–4794.
[60] a) J. H. Yoon, H. C. Kim, C. S. Hong, *Inorg. Chem.* **2005**, *44*, 7714–7716; b) H.-Z. Kou, S. Gao, B.-W. Sun, J. Zhang, *Chem. Mater.* **2001**, *13*, 1431–1433; c) H.-Z. Kou, W.-M. Bu, S. Gao, D.-Z. Liao, Z.-H. Jiang, S.-P. Yan, Y.-G. Fan, G.-L. Wang, *J. Chem. Soc. Dalton Trans.* **2000**, 2996–3000; d) C. Aoki, T. Ishida, T. Nogami, *Inorg. Chem.* **2003**, *42*, 7616–7625.
[61] J. Lefebvre, S. Trudel, R. H. Hill, D. B. Leznoff, manuscript in preparation.
[62] T. Roisnel, J. Rodriguez-Carvajal, *Proceedings of the Seventh European Powder Diffraction Conference (EPDIC 7)*, Trans Tech Publications, Switzerland, **2000**, pp. 118–123.
[63] W. Kraus, G. Nolzeb, *J. Appl. Crystallogr.* **1996**, *29*, 301–303.
[64] E. J. Gabe, P. S. White, G. D. Enright, *DIFRAC: A Fortran 77 Control Routine for 4-Circle Diffractometers*, National Research Council, Ottawa, **1995**.
[65] E. J. Gabe, Y. LePage, J.-P. Charland, F. L. Lee, P. S. White, *J. Appl. Crystallogr.* **1989**, *22*, 384–387.
[66] P. W. Betteridge, J. R. Carruthers, R. I. Cooper, K. Prout, D. J. Watkin, *J. Appl. Crystallogr.* **2003**, *36*, 1487.
[67] L. J. Farrugia, *J. Appl. Crystallogr.* **1997**, *30*, 565.
[68] T. D. Fenn, D. Ringe, G. A. Petsko, *J. Appl. Crystallogr.* **2003**, *36*, 944–947.
[69] M. K. Ehlert, S. J. Rettig, A. Storr, R. C. Thompson, J. Trotter, *Can. J. Chem.* **1989**, *67*, 1970–1974.

Received: March 4, 2006
Published online: August 3, 2006

